

Chapter 10

Mechanistic Aspects of Fracture

II—Plasticity-Dominated Fracture Models



10.1 Outline of Elemental Concepts of Ductile Fracture

The contrastive picture to decohesion is the so-called microvoid coalescence (MVC) that designates the process in which fracture proceeds by the successive nucleation, growth, and linkage of voids. Dimple patterns characterize the surface of MVC fracture. Historically, MVC addressed dimple fracture of the optical microscopy scale. However, the MVC process can proceed on a very fine scale, even under macroscopically irregular or crack-like appearances. Most theories of ductile fracture address the growth and coalescence process, but the void or crack nucleation and its precursory process seriously affect the final fracture.

10.1.1 Void Nucleation

(a) Second phase particles

The misfit of plastic displacement between the matrix metal and a second phase particle readily separates the interface when the plastic deformation of the specimen is substantial. Void nucleation at second-phase particles, like non-metallic inclusions and carbides in steel, is commonly observed for various metals and alloys, as documented in a review article [1]. Some theoretical models have been presented for cavity formation from second-phase particles [2, 3]. The criterion proposed by Argon et al. for cavity formation was that the interfacial stress reaches the ideal shear strength of the interface provided that sufficient elastic energy available to create new surfaces is stored [2]. The size and distribution of particles are parameters in the criterion originating in interactions of stress fields produced by particles. Argon et al. noted that small cavities less than about 100 nm are difficult to open up spontaneously because the stored elastic energy is insufficient.

The energy criterion for the formation of cavity at a particle by interface separation is,

© The Author(s), under exclusive license to Springer Nature Singapore Pte Ltd. 2023
M. Nagumo, *Fundamentals of Hydrogen Embrittlement*,
https://doi.org/10.1007/978-981-99-0992-6_10

265

$$\Delta E_{\text{el}} + \Delta E_s \leq 0, \quad (10.1)$$

where ΔE_{el} and ΔE_s are, respectively, the internal elastic energy of the particle and the energy increase in forming the new internal surfaces [3]. ΔE_{el} is a function of the stress acting on the particle. Goods and Brown expressed the criterion in terms of the critical strain taking into account the local stress exerted by dislocations near the particle [3]. The critical strain is proportional to the particle size and depends on the particle shape, coarseness of slip, and temperature.

A model of the crack formation by dislocation pileup at small particles like carbide is Eq. (9.36) described in Sect. 9.4.2b. The model was originally for an incipient crack in brittle fracture supposing grain-boundary carbides. For the plasticity-dominated fracture to proceed, a dense distribution of small particles must be present.

(b) Dislocation reactions

Two models of the dislocation-originated crack formation are shown in Fig. 9.2, both as an incipient crack for brittle fracture. Stroh's model assumed pileup at grain boundaries of dislocations moving along a slip band. Difficulties of the model in operating as an incipient crack in hydrogen-induced brittle fracture are described in Sect. 9.1b, and the nanoscale cracks predicted by the models in Fig. 9.2 have not been observed experimentally.

(c) Vacancy agglomeration

Fine dimples not associated with second-phase particles are often present, and void nucleation without second-phase particles was revealed at the grain and twin boundaries in titanium alloys [1], at the crack front in AISI 310 stainless steel foils [4], and in high-purity single-crystal silver foils [5]. Intense strain localization characterizes the sites for the void nucleation, and a viable origin of voids is the condensation of vacancies [4]. Vacancy generation associated with plasticity is described in Sect. 3.2.1.2, and the calculated concentration of vacancies generated by jogged dislocations is shown in Fig. 3.3 [6] as a function of axial plastic strain. Excess vacancies might diffuse away or annihilate at sinks, but Cuttiño and Ortiz pointed out possible mechanisms to stabilize vacancy aggregates [6]: (1) the reduction in the free energy of the system by condensation of vacancies into clusters or voids and (2) the reduction in the surface energy by chemisorption of impurity gas such as oxygen. However, the size of vacancy clusters is still very small, and some mechanisms must operate to induce their growth and/or their link with the main crack. Interaction with hydrogen reduces vacancy formation energy and diffusivity of vacancy clusters, as described in Sects. 3.2.2 and 3.2.3.

Refinement of the dimple size characterizes the fracture surface in hydrogen embrittlement, and the dimple shape distorts to irregular quasi-cleavage with increasing hydrogen degradation, as described in Sects. 7.2.2 and 7.2.3. Fractographic features denote the void nucleation, growth, and coalescence in the crack propagation process, due to the evolution of deformation microstructures and resultant lattice imperfections.

10.1.2 Void Growth and Coalescence

10.1.2.1 Mechanistic Effects

Stress states are crucial in void growth. McClintock calculated the deformation of fully plastic materials containing sets of cylindrical holes of an elliptical cross-section in the regime of continuum mechanics [7]. The model was for a hole of semiaxes a and b , with a cylindrical axis in the z -direction, surrounded by a cylindrical cell whose dimensions are the order of the mean spacing between the holes. For plane-strain deformation of a hole in an infinite media, the relative growth factor is defined as

$$F_{zb} = \left(\frac{b}{l_b} \right) / \left(\frac{b^0}{l_b^0} \right), \quad (10.2)$$

where b , l , and the superscript 0 denote radius, spacing, and the initial value, respectively. The fracture condition is that the growth of the holes is such that each hole touches a pair of its cell walls. The relative hole-growth factor at fracture due to z holes growing together in the b direction is

$$F_{zb}^f = \left(\frac{1}{2} \right) / \left(\frac{b^0}{l_b^0} \right). \quad (10.3)$$

The fracture occurs on the ij -plane when the ij growth factor is the first to reach F_{ij}^f . For tests with a varying stress history, the fracture was thought to occur when accumulation of “damage”, defined as

$$d\eta_{ij} = d(\ln F_{ij}) / \ln F_{ij}^f, \quad (10.4)$$

reaches unity.

The hole growth with increasing strain was calculated using F_{zb} for viscous and plastic materials under different stress ratios. Stress triaxiality and strain hardening strongly affect fracture strain. Strain hardening is expressed as

$$\bar{\sigma} = \sigma_1 \bar{\epsilon}^n \quad (10.5)$$

for equivalent stress $\bar{\sigma}$ and strain $\bar{\epsilon}$. The smaller n enhances the more pronounced hole growth. An approximate expression of the increase in damage with increasing strain was

$$\frac{d\eta_{zb}}{d\bar{\epsilon}} = \frac{\sinh \left[(1-n)(\sigma_a + \sigma_b) / (2\bar{\sigma} / \sqrt{3}) \right]}{(1-n) \ln F_{zb}^f}. \quad (10.6)$$

When the ratios between components of applied stress are constant, integration of Eq. (10.6) gives the fracture strain required for z -axis holes to coalesce in the b direction as

$$\bar{\varepsilon}^f = \frac{(1-n)\ln(l_b^0/2b^0)}{\sinh\left[(1-n)(\sigma_a + \sigma_b)/(2\bar{\sigma}/\sqrt{3})\right]}. \quad (10.7)$$

Equations (10.6) and (10.7) indicate that the transverse principal stress strongly reduces fracture strain rather than solely the mean stress or the maximum principal stress. The equations also show the interaction between stress triaxiality and strain hardening, and the effect of triaxiality is significant for the smaller hardening exponent.

The onset of necking in tensile straining of materials is a crucial stage in ductile fracture. Thomason applied this notion to the local coalescence of voids within materials [8, 9]. His internal necking model is schematically shown in Fig. 10.1 [8] for initially a square array of small square holes in a plane-strain plastic field. The material is non-hardening rigid-plastic under the hydrostatic pressure P . A tension applied in the X_1 direction causes the deformation of holes. Deformation of the region between adjacent holes is constrained by the outer regions of the holes, against necking occurring. Straining changes the constraint associated with the change of the hole geometries.

The condition of unstable plastic flow to begin is that the load L_u for uniform flow exceeds the load L_n to cause internal necking. The mean tensile stress σ_n in the X_1 direction to start internal necking was given as,

$$\sigma_n(1 - \sqrt{V_f}) + P < \sigma_{22} + 2\tau_y, \quad (10.8)$$

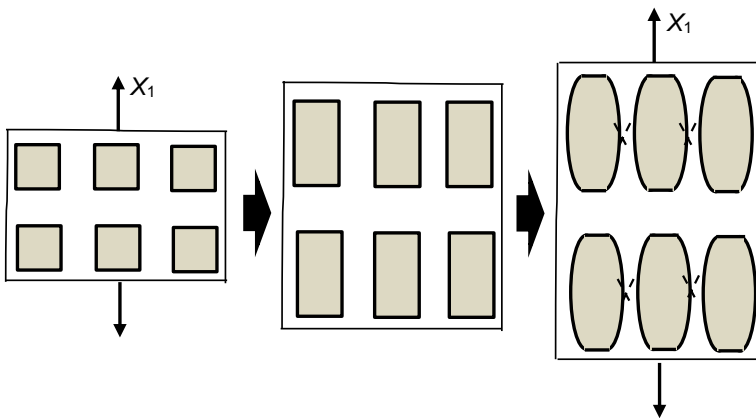


Fig. 10.1 Model of void linking by internal necking. Initially, a square array of small square holes is placed within a matrix (After Thomason [8])

where V_f is the volume fraction of holes, σ_{22} is any tensile stress applied in the X_2 direction, and τ_y is the yield shear stress. Effects of V_f , P , and σ_{22} on the post-instability strain, i.e., the amount of strain from the onset of macroscopic instability to the start of internal necking, were computed. Strain after the instability is significantly reduced by increasing V_f and σ_{22} while the hydrostatic pressure P suppresses the reduction.

The operating stress fields are crucial in void growth. Gurson proposed a constitutive relation for porous material in terms of the yield function Φ [10, 11], and its form modified by Tvergaard for the bifurcation instability problem is

$$\Phi = \frac{\sigma_{\text{eqv}}^2}{\sigma_y^2} + 2f q_1 \cosh\left(\frac{3q_2 \sigma_m}{2 \sigma_y}\right) - (1 + q_3 f^2) = 0 \quad (10.9)$$

where σ_{eqv} is the equivalent tensile stress, σ_y is the matrix flow stress, σ_m is the macroscopic mean stress, f is the void volume fraction, and qs are numerical parameters [12]. $\Phi = 0$ must be satisfied at any stage of the deformation.

Needleman and Tvergaard applied Eq. (10.9) to ductile fracture of materials containing voids, adopting $q_1 = q_3 = 1.5$ and $q_2 = 1$ [13]. Equation (10.9) implies that the increase in the void volume fraction lowers flow stress. The void volume fraction f increases during straining by the nucleation of new voids and the growth of existing voids. Then, the increasing rate \dot{f} consists of two terms,

$$\dot{f} = \dot{f}_{\text{nucleation}} + \dot{f}_{\text{growth}}. \quad (10.10)$$

The form of each term in the right-hand side was,

$$\dot{f}_{\text{growth}} = (1 - f) G^{ij} \dot{\eta}_{ij}^p, \quad (10.11)$$

and

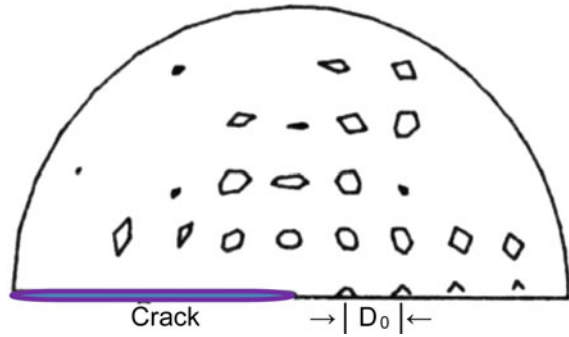
$$\dot{f}_{\text{nucleation}} = B(\dot{\sigma}_y + \dot{\sigma}_m) + D \dot{\varepsilon}_M^p. \quad (10.12)$$

where G^{ij} is the metric tensor that defined the stress deviator $s^{ij} = \sigma^{ij} - G^{ij} \sigma_m$, $\dot{\eta}_{ij}^p$ is the plastic part of the macroscopic strain rate, and $\dot{\varepsilon}_M^p$ is the effective plastic strain rate. For the plastic strain-controlled void nucleation, the increasing rate of void volume fraction was written as,

$$\dot{f}_{\text{nucleation}} = \frac{f_N}{s_N \sqrt{2\pi}} \exp\left[-\frac{1}{2} \left(\frac{\varepsilon_M^p - \varepsilon_N}{s_N}\right)^2\right] \dot{\varepsilon}_M^p, \quad (10.13)$$

where f_N is the volume fraction of void nucleating particles, ε_N is the mean strain for nucleation, and s_N is the corresponding standard deviation. For the stress-controlled void nucleation with the mean stress σ_N for nucleation,

Fig. 10.2 The distribution of large particles near the initial crack tip in model material. Contours depict a constant value ($= 0.004$) of the stress-controlled void nucleation amplitude f_N in Eq. (10.18). D_0 is the initial distance between particles center (Needleman et al. [13])



$$\dot{f}_{\text{nucleation}} = \frac{f_N}{s_N \sqrt{2\pi}} \exp \left[-\frac{1}{2} \left(\frac{(\sigma_y + \sigma_m) - \sigma_N}{s_N} \right)^2 \right] (\dot{\sigma}_y + \dot{\sigma}_m). \quad (10.14)$$

The model material that Needleman and Tvergaard employed contained two types of particles: large particles that nucleate voids at relatively small strains and small particles that nucleate voids at much greater strains. The former and the latter imagined large second-phase particles and fine precipitates, respectively. The large particles were placed in regular arrays, and the void nucleation was assumed stress-controlled. On the other hand, small particles were uniformly distributed and the void nucleation was strain-controlled. Figure 10.2 [13] shows an example of the model distributions of large particles near the initial crack, which is represented by a semicircular notch. Contours in the figure denote a constant value ($= 0.004$) of the volume fraction of void nucleating particles, and D_0 is the initial distance between particle centers.

Stress and strain fields were computed using a finite element method, and the crack growth in ductile fracture was ascribed to the coalescence of the nearest large void with the crack tip. Ductile fracture is dominated by the interaction between the crack tip and the nearest large void or between two neighboring large particles. An important implication is that the strain-controlled nucleation of small voids in the ligament between the crack tip and the large void is crucial and that the void volume fraction remains very low in the material near the surface of the growing crack. The coalescence criterion was that the void volume fraction in the ligament reaches a critical value, implicitly imaging the loss of the stress-carrying capacity.

Events ahead of the crack tip are crucial for fracture toughness when strain localization dominates the crack advance. Needleman-Tvergaard's model addressed the coalescence of the crack tip with the nearest large void. Gao et al. assumed arrays of voids, different in initial shapes, volume fractions, and distributions, in front of the crack [14]. Gao et al. analyzed the growth and coalescence of multiple voids using a finite element method under a three-dimensional, small-scale yielding condition. Interaction among multiple voids elevates the void growth rate and accelerates the

failure process. A fracture criterion Gao et al. used was the critical ligament reduction ratio, defined as the ratio of the current ligament length (the shortest distance between two adjacent voids in the x -direction) to the initial ligament length.

10.1.2.2 Microscopic Process

Besides the above mechanistic consideration for voids, void growth takes microscopic steps. Cuttiño and Ortiz considered the growth of a nanovoid surrounded by supersaturated vacancies generated by plastic deformation [6]. Assuming the void growth by successive diffusing-in of vacancies, the void radius a during the time interval Δt is

$$\Delta a = \frac{1}{a} D(c_0 - c_s) dt, \quad (10.15)$$

where D is the diffusion coefficient of vacancy, and c_0 and c_s are, respectively, vacancy concentrations in remote areas and at the boundary of the void. In the limiting case of $c_0/c_s \ll 1$, the void radius grows as the square root of time.

Cuttiño and Ortiz further considered that the condition which separates ductile from brittle behavior is whether voids can be nucleated before critical stress is reached on the cleavage planes. A void formed in the vicinity of the crack tip grows with the increasing applied stress intensity factor K to a critical size, which is considered to be comparable to the mean spacing $1/\sqrt{\rho}$ between dislocations. A void of this size can grow by continuum plasticity and quickly coalesces with the crack. In the case of a Cu bicrystal, assuming $10^{-6} \text{ m}^2/\text{s}$ for D and about 54 s for the time until reaching the critical size, the void growth was predicted from the initial radius 0.6 nm to the maximum $230b$ (b : Burgers vector) with the vacancy concentration of 6.3×10^{-5} . The assumed magnitude of D was very large as the value at room temperature, and Cuttiño and Ortiz postulated pipe diffusion of vacancies along dislocation lines.

Vacancy migration is not the sole mechanism of void growth; the material transfer by dislocation emission from the void surface expands the void. Traiviratana et al. precisely analyzed the process from a nanovoid in fcc copper using molecular dynamics (MD) simulations within the framework of embedded atom method (EAM) potential [15]. For a single crystal, the domain was $10 \times 10 \times 10 \text{ nm}$ with 1 nm radius spherical void at the center, i.e., 0.42% in the void volume fraction, which was kept constant during the calculation. For a bicrystal domain, two single-crystal cubes shared a tilt boundary making an angle of 43.6° , with a nanovoid of 18 nm in radius placed on the grain boundary. Uniaxial tensile volume strain was applied at a strain rate of $10^8/\text{s}$ without the involvement of diffusion. Visualization of stacking faults represented dislocations.

The calculated stress–strain curves exhibited stress-drops corresponding to the emission of shear loops. The stress drop was significant, but its amount decreased with increasing void radius in the 0.5–4 nm range. Voids grow by the sequential nucleation, growth, and expansion of shear loops from the void surface, and shear

loops in intersecting $\{111\}$ planes react without trailing stationary dislocation. The dislocation density around an expanding void was as high as 10^{11} – $10^{12}/\text{cm}^2$.

Chandra et al. developed simulations in single-crystal copper for the case when multiple nanovoids are present [16]. A cubical domain was oriented along $[100]$, $[010]$, and $[001]$, and the side length of cube was varied from 10 to 22 nm. Firstly, a cylindrical void was inserted in the center, and the diameter of the void was varied with cell size to keep a constant initial void volume fraction of 0.5%. Uniaxial expansion strain was applied along the x -direction at a strain rate of $\approx 10^8/\text{s}$.

On increasing the applied stress, disordered atoms appeared at the void surface, and the first embryo of the leading partial dislocation was detached from the void surface into the matrix. Two partial dislocation embryos punched out from the void eventually formed two shear dislocation loops on $\{111\}$ planes. Continuous application of load increased the amount of shear loops, and the partial dislocations gliding on different slip planes interacted to form a Lomer-Cottrell stair-rod dislocation, sessile in nature. At large strains, the simulation box contained a forest of partial dislocations and stair-rods.

In the case of heterogeneous void distribution, disordered atoms first appeared around the largest void, and the continuous load application emanated dislocation loops from the neighboring voids. As a result, the voids coalesced into a single and larger void, marking the process of void coalescence. This ultimately reduced the load carrying capacity of the material until final failure. Figure 10.3 [16] depicts the process.

The size and distributions of nanovoids are crucial for operating the above scheme. Some conditions inevitably presumed in MD simulations, like strain rate and temperature, are apart from practical situations. However, the depicted process is indicative of an autocatalytic process of nanovoid formation and dislocation activity in ductile

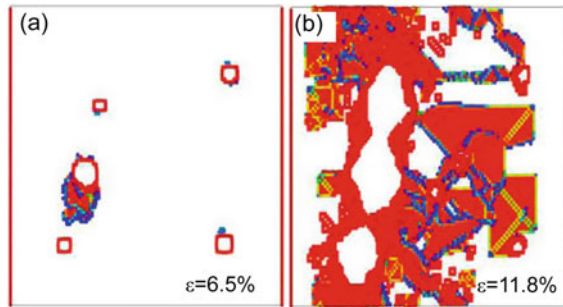


Fig. 10.3 Molecular dynamics simulation snapshots showing the microstructural evolution of single-crystal Cu containing 5 voids of random size and distribution with the initial void volume fraction of 5%. **(a)** Evolution of dislocation loops from the largest void, along with appearance of disordered atoms at the surfaces of other voids. **(b)** Coalescence between voids, which ultimately leads to further void coalescence in the system. Atoms are colored according to their centro-symmetry parameter; only atoms in the non-centrosymmetric environment are shown (Chandra et al. [16])

fracture. When the nanovoid density is substantial, dislocations emitted from neighboring nanovoids interact to produce new nanovoids that sequentially coalesce. The process will be viable in a late stage of plastic deformation where a high dislocation density causes substantial mutual interactions of dislocations. The models presumed the coexistence of high densities of dislocations and vacancies without including hydrogen. The models are general ones of the plasticity-controlled fracture, but the presence of hydrogen likely promotes the process leading to fracture.

10.1.2.3 Crack Growth Resistance and Its Microscopic Origin

Afore-cited studies discussed the void nucleation and growth during crack advance associated with plasticity in continuum mechanics or regular lattice regimes in the crack front region. As described in Sect. 6.2.2.3, the crack growth resistance curve, *R*-curve, links the total energy dissipation rate and microscopic fracture processes through the constitutive relation in calculating the *J*-integral. *R*-curve reflects internal changes causing the energy dissipation during the crack advance. When strain localization is substantial, most of the energy dissipation relevant to the crack advance must occur in the crack front region, where deterioration of crystallinity is substantial.

The *R*-curve of steel is susceptible to microstructures. Figure 10.4 [17] shows *R*-curves obtained by three-point bend tests of three 0.08 mass % C ferrite–pearlite model steels of about 450 MPa in tensile strength. The three steels contain 2 mass % of (Mn + Ni) with varied Mn/Ni ratios, and the compositions resulted in different amounts of carbides along grain boundaries. The steel in Figs. 6.15 and 7.5 is Steel B and Steel A, respectively, used in Fig. 10.4. The Ni content was 2.06, 0.98, and 0.01 mass %, respectively, in Steel A, B, and C. The microstructures of the steel were characterized by the presence of carbides along grain boundaries. The grain-boundary carbides constrain slip extension, causing substantial strain localization. The constraint factor, η , was defined as

$$\eta = \frac{L_c}{2L_f + L_c}, \quad (10.16)$$

where L_c and L_f are the ferrite boundary lengths of with or without constraint phases such as carbides, pearlite, and bainite grains. The values of η are 58.1, 33.2, and 43.5% for steel A, B, and C, respectively.

A critical issue is the function of the constraint phases on *R*-curves. Lattice defects induced by plastic straining were detected using hydrogen as the tracer. Figure 10.5 [17] shows thermal desorption curves of tracer-hydrogen (tritium in this case) introduced to the three steels strained to 20% at room temperature. Hydrogen (tritium) absorption capacities were almost identical in the three steels without straining. When given plastic strain, the amounts of tracer-tritium were more significant in steel with the higher constraint factors, and the tracer-tritium was diffusive, i.e., weakly trapped in dislocations and vacancies, at room temperature.

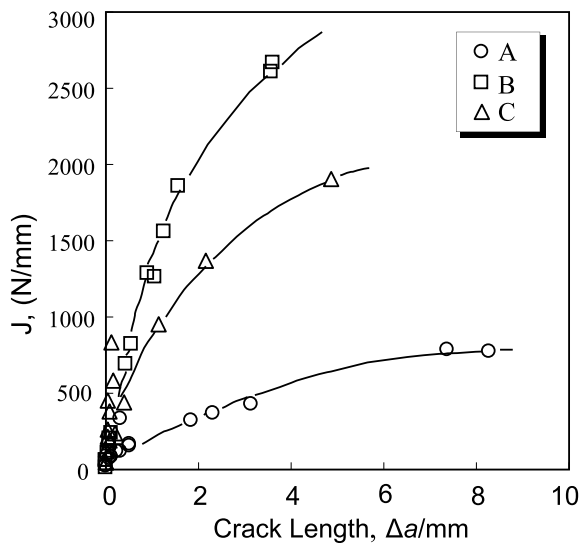


Fig. 10.4 *R*-curves of three low-carbon steels of similar compositions except Mn/Ni ratios for 2 mass % of (Mn + Ni). Three steels have different constraint factors for slip extension across grain boundaries. Tests are conducted at 293 K (20 °C) (Nagumo et al. [17])

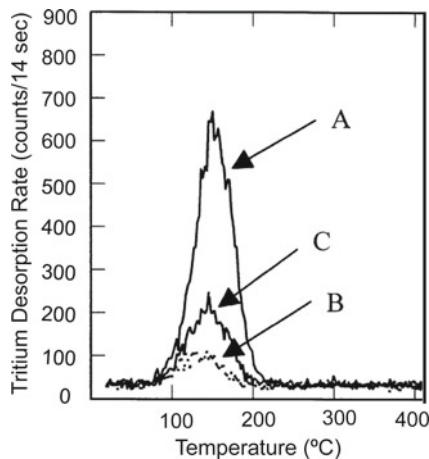
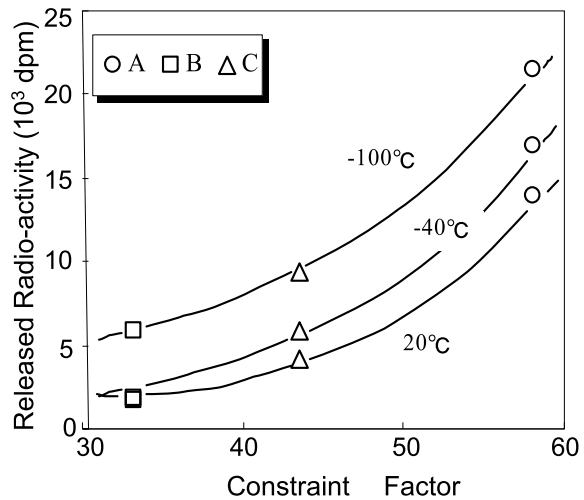


Fig. 10.5 Thermal desorption profiles of tritium introduced to the three steels used in Fig. 10.4 strained to 20% at 293 K (20 °C) (Nagumo et al. [17])

Figure 10.6 [17] plots the amounts of tracer-hydrogen in terms of the released radio-activity (disintegration per minute, dpm), as a function of the constraint factor for specimens strained to 20% at different temperatures. The amounts of tracer-hydrogen correspond to those of strain-induced defects. The results indicate that the constraint of slip extension, likely due to grain-boundary carbides, causes strain

Fig. 10.6 Correlation between the constraint factor and the total amount of the thermally desorbed tritium from the three steels in Fig. 10.4 strained to 20% at different temperatures (Nagumo et al. [17])

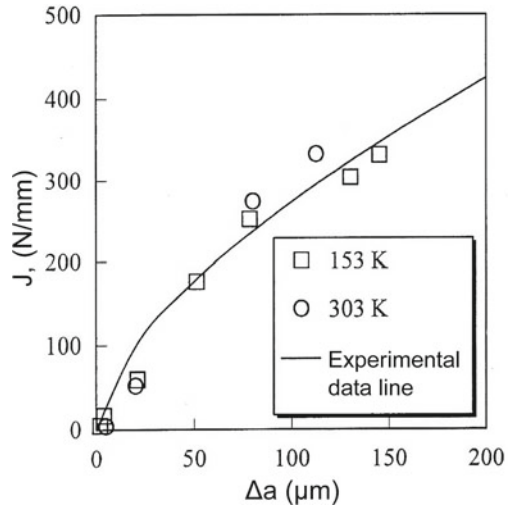


concentration, and mutual interactions of dislocations enhance the creation of strain-induced vacancies that trap tracer-hydrogen. A high density of vacancies leads to vacancy clusters and void formation, promoting fracture to proceed. In this experiment, the observed tritium amount was the average of the entire specimen, not the local one near the crack front. However, the constraint effects are more viable in the crack front, and the dominant role of strain-induced damage in the R -curve, or in the crack advance, will still hold.

This notion was further examined by a simulation of the R -curve. J -integral is experimentally evaluated from the specimen geometries and the load versus load-point displacement curve area, as described in Sect. 6.2.1.2. On the other hand, J -integral is calculated from the stress and strain fields near the crack tip. Yoshida computed the stress and strain fields near the crack tip by means of a finite element method using Gurson-Tvergaard's constitutive relations for porous materials, Eq. (10.9), and experimentally obtained flow stress [18]. Equation (10.13) was adopted to calculate the plastic strain-rate-controlled void nucleation rate, using experimentally determined volume fractions of void nucleating particle, f_N . Void nucleating particles were hard phases such as cementite layer or pearlite existing along grain boundaries, and f_N was measured by scanning electron microscopy on a vertical cross-section of specimens subjected to tensile straining up to ε_N just before the maximum stress. The experimental value of f_N for Steel B was 0.02.

The J -integral values were calculated at successive extensions of a crack, and Fig. 10.7 [18] plots calculated J -integral values on the experimental R -curves for Steel B in Fig. 10.4 at two test temperatures. The agreement between the calculation and experiment is satisfactory. An insensitivity to the test temperature is a characteristic feature of the R -curve. The simulation of the R -curve in Fig. 10.7 validated the feature, and the reason is the opposite temperature dependencies of the flow stress and strain, canceling each effect on the buildup of strain energy for J -integral [18].

Fig. 10.7 Comparison between calculated and experimental R -curves for Steel B in Fig. 10.4 tested at different temperatures (Yoshida et al. [18])



10.1.3 Model of Plastic Instability

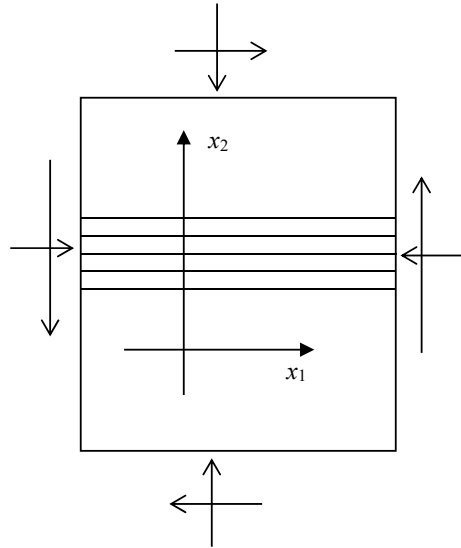
Localized progress of plastic deformation without an increase in the applied load is a critical stage preceding the crack initiation in fracture. Plastic instability also plays a crucial role in void coalescence, as shown in Fig. 10.1 for Thomason's model for internal necking. Plastic instability that appears in hydrogen embrittlement is described in Sect. 7.3.3 concerning strain localization. Onyewuenyi overviewed various factors influencing premature failure associated with plastic instability [19]. Factors that induce plastic instability are: materials flow in specific crystallographic planes and directions, and microstructural or geometrical inhomogeneities such as inclusions, voids, and free surfaces. In continuum mechanics, jump discontinuities in displacement gradient across certain surfaces, like shear bands, characterize plastic instability in homogeneous deformation.

Regarding fracture of brittle rock under compressive principal stresses, Rudnick and Rice assumed that instability is a bifurcation from the homogeneous deformation of an initially uniform material to the non-uniform localized deformation into a planar band [20]. The model is likely general as an incipient non-uniform field, and deformation rates vary with positions across the band but remain uniform outside the band. The coordinate system for the band is shown in Fig. 10.8 [20].

The macroscopic constitutive relation of the material is crucial. For the material, Rudnick and Rice adopted elastic–plastic constitutive relations in a pressure and temperature regime, showing apparent macroscopic inelastic strain and dilatancy. Shear and volumetric strain increments $d\gamma$ and $d\varepsilon$, respectively, and their plastic portions, $d^p\gamma$ and $d^p\varepsilon$, are written as

$$d\varepsilon = -(d\sigma/K) + d^p\varepsilon, \quad d\gamma = (d\tau/G) + d^p\gamma, \quad (10.17)$$

Fig. 10.8 Coordinate system for the band of localization (Rudnicki et al. [20])



and

$$d^p \varepsilon = \beta d^p \gamma, \quad (10.18)$$

where σ is the hydrostatic stress, K and G are bulk and shear moduli, respectively, and β is the dilatancy factor. Further, the plastic hardening modulus h is defined as

$$d\tau = h d^p \gamma, \quad (10.19)$$

for constant σ . The shear stress τ versus shear strain γ curve is shown in Fig. 10.9 [20].

The instability condition was derived from the continuity of stress equilibrium, to be satisfied until the start of bifurcation. The hardening modulus h varies by the orientation of the potential plane of localized deformation and plays a crucial role in the instability. The modulus h is a decreasing function of the amount of strain, and h must be the maximum for the orientation of the plane of localization. The instability takes place at the critical value h_{cr} . Stress states, β values, and the slope of the τ versus σ curve determine h_{cr} . Rudnick and Rice noted that the start of rupture was feasibly modeled as a constitutive instability.

10.2 Hydrogen-Enhanced Localized Plasticity Theory

Beachem observed a pronounced decrease in torque by hydrogen in torsion tests of AISI 1020 steel pipe specimens [21], described in Sect. 5.2.2. Simultaneously

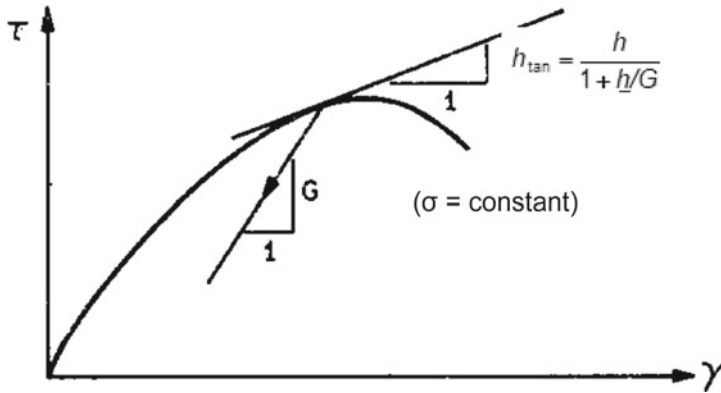


Fig. 10.9 Shear stress τ versus shear strain γ curve showing the geometric interpretation of the hardening modulus h ($= d\tau/d\gamma$), the tangent modulus h_{tan} , and the elastic shear modulus G . γ denotes plastic portion of shear strain (Rudnicki et al. [20])

conducted wedge-loaded compact tension tests for AISI 4340 steel revealed successive changes in the fracture mode with decreasing stress intensity factor, described in Sect. 7.2.5. Beachem postulated that hydrogen in solid solution increases dislocation activity and expands a plastic zone ahead of the crack tip, including more inclusions that act as void nuclei. The model is hydrogen-assisted cracking, HAC, rather than the direct embrittlement by hydrogen in the enhanced lattice decohesion model. However, the effects of hydrogen on macroscopic flow stress are not yet conclusive, and hardening rather than softening has been commonly observed for bulky specimens of commercial-grade steel. Many experiments that exhibit involvement of plasticity in HE, even in apparently brittle-like fractures, are described in Sect. 7.1.

Transmission electron microscopy (TEM) equipped with an environmental cell of hydrogen atmosphere directly demonstrated enhanced mobility of dislocations, as described in Sect. 5.4. It was strong support to claim the primary role of dislocation activity in HE. However, some critical comments are present, e.g., a reduced surface energy by hydrogen might release pinning of dislocation under stress at the foil surface. The hydrogen-enhanced localized plasticity (HELP) has been theoretically rationalized in respect of the shielding of elastic interactions between dislocations and between dislocations and other stress centers, as shown by Eq. (5.12) in Sect. 5.5.1. However, numerical estimations showed that fairly high hydrogen concentrations over 0.01 are necessary to exhibit the shielding effects by hydrogen. First-principles calculations have been conducted on interactions between hydrogen and screw dislocations, Sect. 3.1.2, and on the mobility of dislocations, Sect. 5.5.2. In many calculations, softening and hardening are not exclusive depending on the setup of the calculation model.

The defect acting agent (DEFACTANT) mechanism by Kirchheim, described in Sect. 3.1.2 for stabilizing lattice defects by hydrogen, is a general concept from

a thermodynamic viewpoint. With respect to HELP, the DEFACTANT mechanism predicts that the decrease in the formation energy by hydrogen activates dislocation sources [22]. It was then deduced that newly generated dislocations push former dislocations together with the ease of kink-pair formation and that the sequence appears as the observed enhanced mobility of dislocations by hydrogen [23].

The HELP mechanism is viable by cases, but the enhanced dislocation mobility *per se* is a deformation mechanism, not the mechanism of fracture. As described in Sect. 7.2.3, Martin et al. postulated that forming very small ~50 nm mounds immediately beneath the QC fracture surface of pipeline steel is a consequence of either near-surface relaxations of newly created surfaces or reflections of underlying dislocation structures [24]. However, the proposed function of HELP in forming the mounds is to prepare high dislocation densities and hydrogen concentrations, and the crack initiation mechanism is another matter to be examined [24].

Precipitation of high-pressure molecular hydrogen is not feasible in usual conditions. Strain discontinuities brought about at internal boundaries or deformation bands are viable to create voids, as Nibur et al. postulated [25], but the conditions for the void nucleation, such as Eq. (10.1), must be satisfied. Further, close examinations of similar fracture surfaces by Neeraji et al. revealed nanovoid nucleation and growth [26], rather than the “mound-on-valley” separation that Martin et al. claimed. The findings are against the interface separation induced by strain discontinuity resulting from the HELP mechanism.

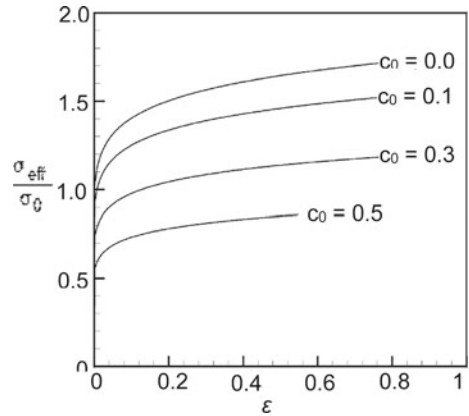
A notion that relates the HELP mechanism to promoted fracture is a synergistic interplay of the HELP and HEDE mechanisms proposed by Novak et al. for cracking of a grain-boundary carbide caused by dislocation pileup [27], described in Sect. 9.4.1. There, the final fracture criterion was essentially that of brittle fracture models. The idea was extended as the HELP-mediated decohesion model to mound-like quasi-cleavage fracture surfaces of pipeline steels [24]. The model postulates that hydrogen transported by activated dislocations causes decohesion at grain boundaries or martensite lath boundaries [28, 29]. However, no reliable experimental evidences for hydrogen transport by moving dislocations are present in iron as described in Sect. 4.3.2.

On the other hand, a mechanistic consequence of the HELP mechanism to promote fracture was presented by Liang et al. [30], following the theory of plastic instability presented by Rudnicki and Rice [20]. Liang et al. employed a constitutive relation to express the flow stress σ as a function of the total hydrogen concentration c (in H/M) in the form

$$\sigma(\varepsilon^p, c) = \sigma_0(c) (1 + \varepsilon^p \varepsilon_0)^N, \quad (10.20)$$

where $\sigma_0(c)$ is the yield stress, ε^p is the effective plastic strain, ε_0 is the yield strain, and the hardening exponent N was assumed to remain unaltered by hydrogen. The form of $\sigma_0(c)$ was tentatively assumed using a softening parameter ξ in the form

Fig. 10.10 Normalized effective stress σ_{eff} versus plastic strain ε^p curves at various initial hydrogen concentrations c_0 calculated using Eqs. (10.20) and (10.21). The hardening exponent $N = 0.1$, the softening parameter $\xi = 0.1$, and σ_0 is the yield stress in the absence of hydrogen (Liang et al. [30])



$$\sigma_0(c) = \sigma_0\{(\xi - 1) c + 1\}. \quad (10.21)$$

Stress–strain curves in terms of the normalized effective stress σ_e/σ_0 plotted against ε^p are shown in Fig. 10.10, taking $\xi = 0.1$, $N = 0.1$, and σ_0 (the yield stress for $c = 0$) = 400 MPa [30].

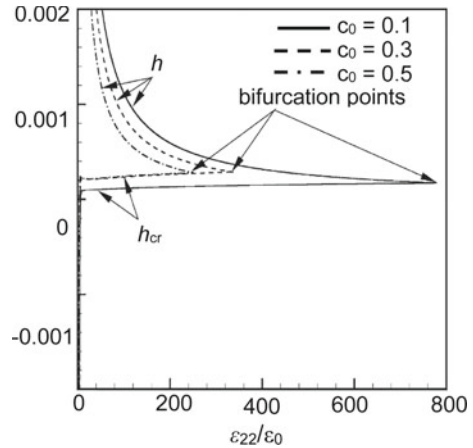
Liang’s model included hydrogen-induced lattice dilatation due to the partial molar volume of hydrogen in the deformation rate tensor. A crucial assumption was that hydrogen is continuously supplied from the environment during the test, keeping the chemical potential of lattice hydrogen constant at c_0 . It was assumed that the total hydrogen concentration c increases with trapping by the increasing density of dislocations during straining. The assumptions imply that trapped hydrogen decreases the flow stress and enhances the decrease in strain hardening. However, corresponding observations of flow behaviors have not been presented.

The employed condition of plastic instability followed Rudnicki-Rice’s model for the bifurcation from continued homogeneous deformation to a localized deformation in a band of intense shear. Results of calculations following Rudnicki-Rice’s procedure are shown in Fig. 10.11 [30] using the hardening modulus h against the normalized applied macroscopic strain for three initial hydrogen concentrations. The modulus h was defined as

$$h = \left[\frac{\partial \sigma_e}{\partial \varepsilon^p} + \left(\frac{\partial \sigma_e}{\partial c} \right) \left(\frac{\partial c}{\partial \varepsilon^p} \right) \right] / 3. \quad (10.22)$$

External tensile stress is applied along the x_2 direction, and the bifurcation occurs when h , which decreases with increasing ε_{22} , reaches the critical value h_{cr} . The higher initial hydrogen concentrations decrease h more promptly, reducing the critical strain for the bifurcation more prominently. Hydrogen-induced softening and lattice dilatation at microscale regions can induce shear localization even though the material as a whole continues to exhibit positive hardening. The idea might be qualitatively reasonable, but Fig. 10.11 indicates that unrealistically high initial hydrogen

Fig. 10.11 Plot of the tangential modulus h and the critical tangential modulus h_{cr} against the normalized applied macroscopic strain $\varepsilon_{22}/\varepsilon_0$ at various initial hydrogen concentrations. The hardening exponent $N = 0.1$ and the softening parameter $\xi = 0.1$, and shear localization occurs when $h = h_{cr}$ (Liang et al. [30])



concentrations, ≥ 0.2 in atomic ratio, are required to cause discernible reductions in the uniform elongation. The misfit with experimental observations might be improved by modifying flow rules, but the consistency with characteristic features of hydrogen embrittlement, such as fracture surfaces described in Sect. 7.2, is a subject to be discussed.

10.3 Adsorption-Induced Dislocation Emission Theory

Fractographic features such as fine, shallow dimples, striations, and quasi-cleavage with steps and tear ridges that characterize hydrogen embrittlement (Sect. 7.2) are quite similar to the features of stress corrosion cracking (SCC) and liquid-metal embrittlement (LME). Since LME occurs even at high crack velocities and for systems of very low mutual solubilities, Lynch proposed that some surface effects, such as the adsorption of hydrogen at crack tips, rather than absorbed hydrogen, play a critical role in hydrogen embrittlement [31, 32]. For LME, adsorption must occur only at crack tips, and Lynch proposed a model that adsorbed hydrogen enhances the injection of dislocations from the crack tip and promotes the coalescence of the crack with voids ahead of the crack.

The elementary fracture mode envisaged is the microvoid coalescence (MVC) process. The qualitative explanation is that adsorbed hydrogen at the crack tip reduces the interatomic strength of metals and facilitates the dislocation nucleation and injection into the bulk. This adsorption-induced dislocation emission (AIDE) mechanism also claims that hydrogen at subsurface sites can contribute to bond weakening. Void nucleation at small and large particles was assumed in areas of large strain, such as localized slip around crack tips, slip band intersections, or dislocation-cell boundaries.

Both the HELP and AIDE mechanisms consider the function of hydrogen in fracture from the viewpoint of strain localization to induce void nucleation. The difference between the two mechanisms is that HELP focuses on enhanced dislocation mobility while AIDE considers the enhancement of the dislocation injection from the surface. The mechanism for transgranular fracture was also applied to apparently smooth intercrystalline facets that exhibited small dimples. Lynch assumed second-phase particles as the void source, but he also noticed the existence of dimples not associated with particles, smaller than dimples produced in air, sometimes difficult to resolve by scanning electron microscopy. However, the origin of such small voids was not pursued. The AIDE model addresses fractographic features at the crack extension, but characteristics of HE are not limited to fractographic features. Hydrogen effects such as strain localization and accumulation of damage in bulk occur before crack initiation, as described in Sect. 7.3.

10.4 Autocatalytic Void Formation and Shear Localization Theory

Flow localization into the shear band induced by plastic instability is a critical stage in ductile fracture, as described in Sect. 10.1.3. In the scheme of continuum mechanics, a low macroscopic strain-hardening rate favors instability. However, very large strain and hydrogen concentrations are necessary to initiate flow bifurcation in a homogeneous material according to a computation-based HELP mechanism, as shown in Fig. 10.11.

On the other hand, microstructural or geometrical inhomogeneities also cause flow localization. Hydrogen effects enhancing strain localization along characteristic slip lines at the U-notch root of a bend specimen of spheroidized steel are shown in Fig. 7.17 in Sect. 7.3.3. Reentrant portions of a roughened surface and particles within slip bands act as trigger sites of plastic instability, but the onset of surface rumpling occurred well before attaining the profuse void formation in bulk [33]. Associated degradation in fracture toughness is shown in Fig. 6.11 in Sect. 6.2.1.2 about mixed mode I/III compact tension tests. It was then deduced that hydrogen's major role was to promote plastic instability before void formation directly [33].

Hirth et al. proposed the autocatalytic model of hydrogen embrittlement, claiming that the nucleation of voids enhances the formation and propagation of shear bands in which voids are further formed [34, 35]. The function of hydrogen was ascribed to promote particle decohesion or cracking at second-phase particles. The model does not require the HELP mechanism that activates dislocations but implicitly assumes high hydrogen fugacity for the interface decohesion to occur. As stated in Sect. 7.3.3, the steel used for experiments had substantial ductility before fracture.

A similar U-notch bend test was conducted for a high-strength AISI 4340 steel of 1.35 GPa in tensile strength. The midspan-deflection at the onset of load drop progressively decreased with the increasing current density of cathodic electrolysis

[36]. In the midplane section of precharged specimens, a narrow mode II crack extended following characteristic slip paths, and the length of the spiral part of the crack increased with decreasing charging current. The extending crack connected to mode I intergranular cracks in a region apart from the notch surface. In contrast to low-strength steel, it was considered that the crack was first initiated internally and connected to the surface. However, the critical notch-root strain at the crack initiation was nearly constant for three different notch-root radii.

It was deduced that the dominant role of hydrogen is to promote plastic instability and that the crack nucleation within the plastic zone is the consequence of a combination of the hydrogen concentration and the total stress. On the fracture surface, MnS was observed at the bottom of large dimples, but the origin of small dimples, which became smaller and more uniform by hydrogen charging, was not definitely mentioned. The experiments that the theory was based were mostly under a high hydrogen fugacity. However, the underlying idea of the autocatalytic model about plastic instability will be general, provided that the void source is not limited to second-phase particles, as described in the following section.

10.5 Hydrogen-Enhanced Strain-Induced Vacancy Theory

Such as crack nucleation in strain-concentrated areas and the crack path along slip planes, many experimental facts presented in Chaps. 5–8 show a deep involvement of plasticity in hydrogen embrittlement (HE). The primary player of plasticity is the dynamics of dislocations, but the functions of dislocations in fracture are multiple. The increase in the density of dislocations and their mutual interactions set up substructures and local stress and strain fields in which fracture events occur. On the other hand, dislocation dynamics also bring about damage that deteriorates the mechanical performance of materials. The term “damage” here broadly denotes disorder or the deterioration of crystallinity rather than flaws such as cracks and voids. The function of hydrogen in embrittlement is to be considered in the context of dislocation dynamics and resultant microstructural changes.

The hydrogen-enhanced strain-induced vacancy (HESIV) mechanism claims that hydrogen enhances the strain-induced generation of vacancies, leading to premature fracture. Excess vacancies are stabilized, and their mobility is reduced by combining with hydrogen, thus forming clusters that act as void sources or reducing the stress-carrying capacity of the material. Figure 10.12 schematically illustrates the creation and clustering of vacancies forming microcracks in a strain-concentrated area close to a barrier for the slip extension. A crucial idea of the HESIV mechanism is to shift the viewpoint on HE from hydrogen per se to hydrogen-related damage that leads to premature fracture, placing the issue on the general plasticity-dominated fracture. The deduced role of hydrogen in the fracture is as a promotor of the deterioration of materials associated with plasticity. Two overview papers summarize the HESIV mechanism in HE of steel [37, 38].



Fig. 10.12 Illustration of the HESIV model for the creation and clustering of vacancies forming microcracks in strain-concentrated area close to a barrier to slip extension

10.5.1 Brief Summary of Findings on Involvement of Strain-Induced Vacancies in HE

(a) Hydrogen-enhanced generation of strain-induced vacancies—TDA and PAS

Utilizing hydrogen trapping in lattice defects, a thermal desorption analysis (TDA) of tritium introduced as the tracer of defects revealed the strain-induced generation of vacancies and its enhancement by hydrogen in iron and steel (Figs. 2.5, 3.2, 3.4, 3.10, 3.11 and 3.14). Positron annihilation spectroscopy (PAS) more directly exhibited the vacancy-type nature of strain-induced lattice defects and clustering of vacancies (Figs. 3.15 and 3.16). A note-worthy fact was that hydrogen *hardly enhanced the increase in dislocation densities by straining* against the HELP theory in a low strain range (Fig. 3.14 and Table 3.5).

Ion-implantation experiments shown in Fig. 3.8 and Table 3.3 validate high densities of vacancies due to the stabilization by hydrogen. Ion-implantation experiments also revealed a decrease in the mobility of vacancies by coupling with hydrogen and forming clusters. Theoretical estimations of high densities of vacancies resulting from mutual interactions of dislocations are described in Sect. 3.2.1.2a. The binding of hydrogen with vacancies reduces the formation energy and then increases the density of vacancies (Sect. 3.2.3.2). Further, first-principles calculations on the mobility of vacancies predicted a high density of vacancies, left behind jog-dragging of screw dislocations by coupling with hydrogen. The findings support the notion that interactions between hydrogen and excess vacancies result in high densities of vacancies and their clusters.

(b) Damage accumulation and stress-history effects

The hydrogen-enhanced decohesion (HEDE) mechanism addresses the function of hydrogen in crack initiation and growth. However, hydrogen-enhanced deterioration of crystallinity proceeds even in stages preceding the onset of cracking, as exhibited in the kernel average misorientation (KAM) (Fig. 8.24) and image quality (IQ) map (Fig. 7.18) in Type 304 stainless steel. The function of hydrogen in embrittlement must be examined over the entire deformation stages.

Damage generated during plastic deformation accumulates and affects the final fracture (Sect. 7.4.2). A decrease in fracture strain by applying cyclic prestressing before tensile tests is shown in Fig. 7.23 for martensitic steel. The presence of hydrogen at prestressing enhanced the degradation (Fig. 7.24), and TDA of tracer-hydrogen exhibited a hump in the desorption peak, indicative of the generation of

vacancy-type defects. In sustained-loading delayed fracture, a conventional notion of the fracture mechanism is an increasing hydrogen concentration to a critical level. However, hydrogen absorbed during sustained loading of high-strength steel did not show a monotonic increase, instead turning to a decrease (Figs. 6.33 and 6.34). On the other hand, the amount of lattice defects increased, indicating the generation of vacancies during the incubation period prior to the onset of fracture (Fig. 7.19). Simultaneously conducted PAS measurement revealed the vacancy-type nature of the defects.

Similarly, giving fatigue cycles promoted fracture in sustained-loading delayed fracture tests of high-strength Si-Cr steel (Fig. 7.25). Annealing at 473 K after pre-fatigued almost eliminated degradation caused by pre-fatigue, indicating that damage generated by pre-fatigue and promoting failure in sustained loading was vacancies. Further, sustained loading in a corrosive environment substantially reduced fracture strain in the successively conducted tensile test for high-strength steel (Fig. 7.26). In this case, the elimination of degradation by 473 K annealing after pre-loading again confirmed the involvement of vacancies rather than dislocations.

(c) Reducing stability of martensitic structures

Stress relaxation of martensitic steel, i.e., a partial release of external stress under a constant-strain condition, is reduced by stabilizing martensitic structures with elevating tempering temperatures (Fig. 5.5 in Sect. 5.3.1). Hydrogen enhances stress relaxation, causing structural instability, but its extent is less in high-strength Mo-V-containing martensitic steel by increasing tempering temperatures and precipitating VC carbides. Concomitantly, the delayed fracture susceptibility of the steel is substantially improved (Fig. 6.28). The total amount of lattice defects is higher, but the fraction of vacancies is less in the VC-containing steel (Fig. 8.5). This corresponds to the effect of tempering of martensitic steel in the susceptibility to HE (Figs. 8.2 and 8.3).

(d) Correlations of strain-induced vacancies with the susceptibility to HE of steel

Compositions and microstructures strongly affect the susceptibility to hydrogen embrittlement of steel even of the same strength levels. Good correlations between the susceptibility and the amount of strain-induced vacancies are demonstrated for high-strength martensitic steel with the prior austenite grain-size effects (Figs. 8.7 and 8.8) and manganese content effects (Figs. 7.6, 7.7, and 8.11). Positron annihilation spectroscopy revealed a more prominent clustering of vacancies in Type 304 austenitic stainless steel than in Type 316L (Fig. 7.22), corresponding to their different susceptibilities to HE.

Strain rate and temperature dependences of the susceptibility to HE, shown in Fig. 6.3, characterize the HE of steel. In tensile tests of cold-worked eutectoid steel, the enhanced degradation by reducing the strain rate was associated with increasing amounts of strain-induced vacancies, as shown in Fig. 6.4. In experiments to investigate cumulative effects of different loading methods, cyclic prestressing in the presence of hydrogen degraded following tensile properties of martensitic steel. The degradation was more prominent with a lower strain rate at cyclic prestressing, as

shown in Fig. 7.23, and the effects of strain rates at cyclic prestressing were well related to the absorption capacity of tracer-hydrogen trapped in vacancies, i.e., the density of strain-induced vacancies as shown in Fig. 7.24.

(e) Observation of nanovoids

Direct observation of void nucleation, growth, and coalescence processes will be the most persuasive to validate a model. Nanoscale processes in areas of high dislocation densities make the observation difficult. However, some transmission electron microscopy (TEM) observations detected nanovoids, like “valley-on-valley” type nanoscale dimples of 5 ~ 20 nm wide and 1 ~ 5 nm deep on QC facets of hydrogen-precharged X65 and X80 line-pipe steel [26] (Sect. 7.2.3), nanovoids within or close to dislocation-cell walls beneath the fatigue-fractured pure iron in high-pressure hydrogen gas (Fig. 7.14), nanovoids in strain localized region, distinguishing from precipitates and dislocation pileup, along QC fracture surface of Al–Zn–Mg–Cu alloys [39] (Sect. 7.3.2).

It is to be noticed that high densities of dislocations and vacancies may distort crystallinity and hinder the imaging of diffracted electrons. Occasional findings of amorphization at the crack front of the crack or beneath the fracture surface of hydrogen-charged iron might be extreme cases (Fig. 7.9).

(f) Critical experiment for the predominant role of vacancies in HE

The afore-described evidence indicates a deep involvement of strain-induced vacancies in HE. The HESIV mechanism remarks the deterioration of materials by plastic deformation, rather than hydrogen itself, to play the primary role in degradation. An experiment that directly demonstrated the decisive role of vacancies in HE was to interpose unloading and reloading during tensile tests of hydrogen-precharged iron and Inconel 625 alloy (Fig. 6.5). The unloading stage was about half or close to the fracture strain. Degassing of hydrogen at room temperature at the unloading stage remained degraded on the successive tensile reloading, while hydrogen was not present at the reloading stage. On the other hand, annealing at 573 K at the unloading stage, removing both hydrogen and strain-induced vacancies, entirely reproduced the original tensile behaviors without hydrogen (Fig. 6.6). It was a direct demonstration of the predominant role of strain-induced vacancies in degradation rather than hydrogen itself.

10.5.2 Mechanistic and Microscopic Functions of Vacancies

(a) Strain localization associated with void nucleation

Hydrogen decreases *R*-curve, as shown in Fig. 6.15 and Ref. [25]. An *R*-curve simulation method is described in Sect. 10.1.2.3 for low-carbon steel of different compositions. The simulation applied Needleman-Tvergaard’s model (Fig. 10.2), which modeled the coalescence of the crack tip with a neighboring void. The condition of

coalescence is that the strain-induced activations of uniformly distributed fine void sources are critical. The model may fit the case where the energy dissipation in the crack front controls the crack extension, as described in Sect. 9.5. J -integral for the simulation was calculated using a Finite Element Method and Gurson-Tvergaard's constitutive relations (Eq. 10.9). Strain localization associated with the crack extension is a characteristic feature of HE (Sect. 7.3). The origin of the different crack growth resistance (R -curve) among steel of different compositions was ascribed to the amounts of strain-induced vacancies, resulting from differences in constraint phases for slip extension (Sect. 10.1.2.3).

For the hydrogen effect on R -curve, Fig. 6.15, the volume fraction of the void nucleation particle, f_N in Gurson-Tvergaard's Eq. 10.10, was increased from 0.02 for the hydrogen-free specimen to 0.035 to make a good fit. The value of 0.02 for the hydrogen-free specimen was experimentally determined for a specimen strained close to the maximum tensile stress. The increase in f_N implies an increase in void volume fraction, and the uniformly distributed and strain-controlled void nucleation, assumed in Needleman-Tvergaard's model, did not exclude vacancy clustering as a void source. The constraint phase in the original microstructure was not affected by hydrogen charging without straining, and the increase in f_N evolves by straining in the presence of hydrogen. The coincidence of experimental and computational results in Fig. 6.15 is consistent with the HESIV mechanism on crack growth.

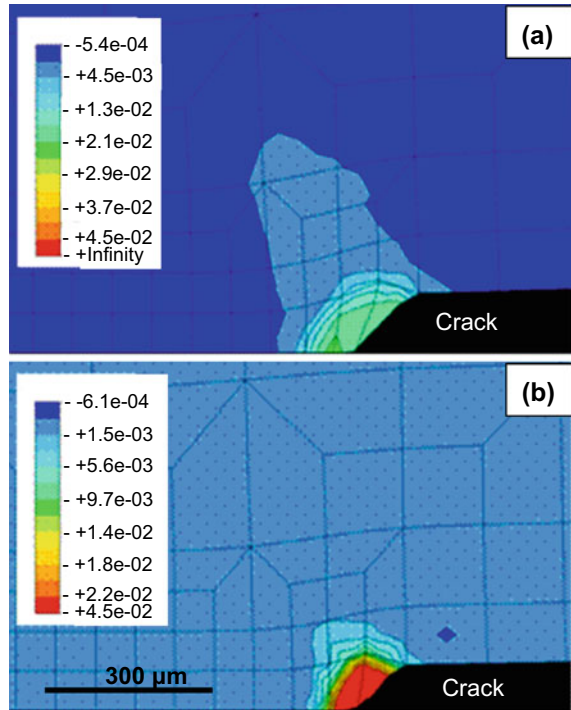
The intense creation of vacancies is closely related to strain localization. The FEM calculation using Gurson-Tvergaard's constitutive relation, Eq. 10.9, exhibited a substantial enhancement of strain localization near the crack tip when hydrogen was present [40]. Distributions of voids ahead of the crack after the advance of 200 μm were computed for Steel B. Figure 10.13 [40] shows the distribution of the volume fraction of nucleation void with and without hydrogen charging. The enhanced localization of voids well explains the fractographic features of HE, such as the refinement of dimple size and quasi-cleavage fracture surface.

(b) Molecular dynamics simulation

Some molecular dynamics (MD) simulations are presented in Sect. 10.1.2.2 concerning dislocation emission from nanovoids and associated void growth and coalescence. The simulations modeled nanoscopic processes of the plasticity-dominated fracture. In the presence of hydrogen, Ding et al. conducted MD simulations for intergranular (IG) fracture of two types of bicrystal nickel with $\Sigma 5(210)[001]$ symmetric tilt or $\Sigma 9(1-10)[22-1]$ pure twist grain boundaries [41]. Each represents typical low- Σ and general grain boundary, respectively. Hydrogen atoms were randomly inserted up to the equilibrium hydrogen distribution in the grain boundary and interior under the same chemical potential. The hydrogen concentration in grains was 0.001 in H/Ni atomic ratio. The simulation box size was $(11.9 \times 23.8 \times 10.6 \text{ nm}^3)$ for $\Sigma 5$ and $(10.6 \times 20.1 \times 9.1 \text{ nm}^3)$ for $\Sigma 9$, respectively. The area 1 nm above and below the grain boundary in the box was referred to as the GB region.

The simulations used the embedded atom method (EAM) potential. By applying uniaxial straining at 300 K, Shockley dislocations nucleated at the GBs and entered into the grains, leaving stacking fault bands along the propagation path. Associated

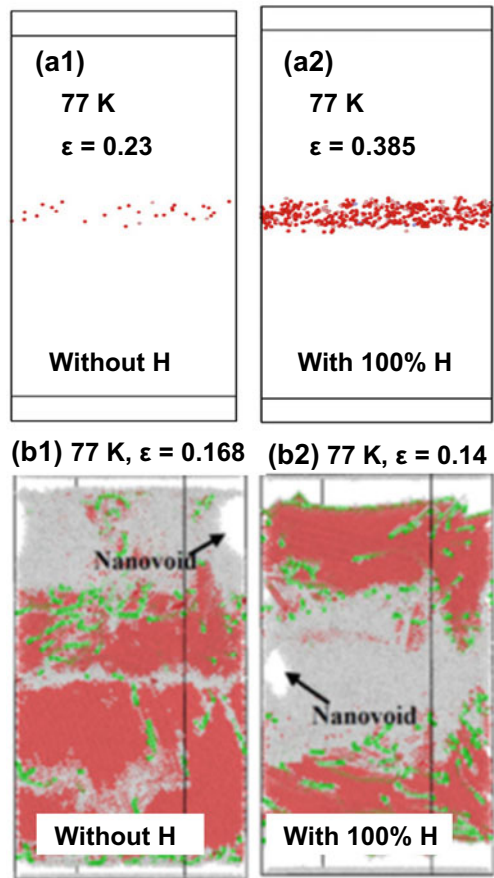
Fig. 10.13 Calculated distributions of nucleation void volume fractions ahead of the crack in Steel B in Fig. 10.4 after the crack advance of 200 μm (a) without and (b) with hydrogen (Nagumo et al. [40])



with the process, distortion of the crystal lattice occurred in the vicinity of GB due to the accumulation of lattice defects. The distortion could be significant, leading to partial amorphization in some local regions. Din et al. defined the distorted atoms with coordination numbers less than nine as vacancy-surface atoms. Figure 10.14(a1) and (a2) are snapshots of the evolution of vacancy-surface atoms in $\Sigma 9(1-10)[22-1]$ boundary, showing hydrogen-enhanced vacancy generation [41]. Further nucleation and emission nucleated nanovoids, eventually leading to fracture along GB. Figure 10.14(b1) and (b2) are snapshots of the hydrogen-promoted process, switching the nanovoid nucleation site from the grain interior to GB. Amorphization of grain boundary shown in Fig. 10.14(b2) likely correspond to the reported findings in Fig. 7.9 of amorphization in the fracture subsurface of hydrogen-charged iron [42] and Type 316L steel [43]. The result also supports the idea that vacancies in the vicinity of GB are potential embryos for nanovoids.

Hydrogen enhancement of vacancy generation depends on temperature. At 77 K, hydrogen enhancement of vacancy concentration in grain boundaries was over ten times. Transgranular fracture prevailed at low vacancy concentrations, but increasing vacancy concentrations led to IG fracture. The critical vacancy concentration for fully IG fracture was 0.17% and 2.8% for $\Sigma 5$ and $\Sigma 9$ grain boundary, respectively. At 300 K, the strain-induced generation of vacancies was observed even without hydrogen, but the hydrogen-enhanced generation was far more significant in vacancy

Fig. 10.14 MD simulation results showing hydrogen-induced transgranular to intergranular fracture transition around $\Sigma 9(1-10)[22-1]$ pure twist grain boundary in Ni. **(a1)** and **(a2)** Snapshots showing vacancy-surface atoms. Only highly distorted atoms with coordination numbers less than 9 in the GB region are colored. FCC atoms are deleted, red HCP atoms indicate the glide paths of $1/6 \langle 112 \rangle$ Shockley dislocations (green pipelines), and grey atoms are in an amorphous structure. The hydrogen concentration is defined as the relative ratio compared to the full saturation cases. **(b1)** and **(b2)** Snapshots showing nanovoid nucleation site switching from grain interior to GB (Ding et al. [41])



than dislocations, favoring the HESIV than the HELP mechanism. However, the prevalence of hydrogen effect on vacancies than dislocations was limited at 600 K.

10.6 Summary of Ductile Fracture Models

Characteristic features HE of steel, like fracture morphologies, crack nucleation sites, crack extension associated with strain localization, and strain rate and temperature effects, indicate a deep involvement of plasticity even for IG fracture of high-strength steel. The function of hydrogen was naturally first focused on dislocations, the primary player of plasticity, to increase either the mobility (HELP) or the density (AIDE and DEFACTANT) of dislocations. However, the mechanistic outcome of activated dislocations is not straightforward in fracture events. Postulated mechanisms are the decrease in the flow stress promoting plastic instability or the

increase in the number of piled-up dislocations resulting in the interface decohesion at second-phase particles.

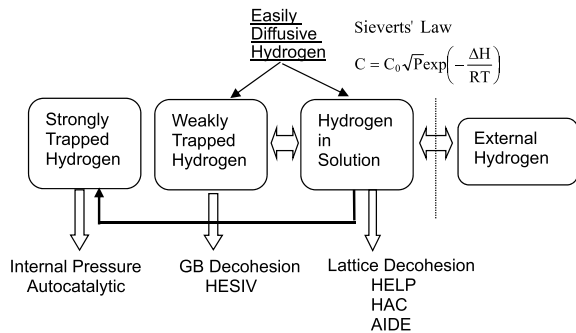
Alternatively, the HELP-mediated decohesion model postulates an enhanced hydrogen transport by activated dislocations to cause grain boundary or interface decohesion. From a mechanistic viewpoint, the autocatalytic model remarks synergistic effects of particle cracking by hydrogen and plastic instability induced by the cracks, resulting in the void sheet formation along slip lines. The viability of a model should depend on situations where the concentration and the fugacity of hydrogen satisfy fracture criteria.

The HESIV model, on the other hand, remarks on the role of vacancies and their clusters as products of activated high-density dislocations. Hydrogen effects are ascribed to stabilizing vacancies by increasing their density and reducing mobility, thus promoting clustering. In fracture events, clustering the high-density vacancies forms void nuclei, and the emission of dislocations from nanovoids is crucial in advancing the cracking process.

Deterioration of local crystallinity is also a matter to be noticed or might be essential. The HESIV mechanism is expected in stages where a substantial activation of dislocations occurs, but the presence of hydrogen is not always necessary to proceed cracking process once substantial amounts of nanovoids and dislocations are prepared. This stage might be general in plasticity-dominated fracture, and the function of hydrogen in HE is like a *promoter of fracture, leading to premature fracture*. The role of hydrogen in fracture is like supplementary. The HESIV mechanism could be applied to the brittle-like fracture, deteriorating the region very close to the crack tip in high-strength steel of high dislocation density.

Major proposed models of the mechanism of HE are placed in Fig. 10.15 [37] concerning the states of hydrogen presumed in each model. Both the HELP and HESIV models premise the role of activated dislocations. The HESIV mechanism must operate under a substantial density of dislocations, and TDA results Figs. 3.2 and 3.4 are the case. However, distinguishing the HELP and HESIV mechanisms is not easy under a high local density of dislocations associated with cracking. Some experimental devices, such as annealing deformation microstructures, will help discriminate the predominant role of either dislocations or vacancies.

Fig. 10.15 Positioning of proposed models for hydrogen embrittlement with respect to states of hydrogen in materials (Nagumo [37])



References

1. R.H. Van Stone, T.B. Cox, J.R. Row Jr., J.A. Psioda, *Int. Metals Rev.* **30**, 157–179 (1985)
2. A.S. Argon, J. Im, R. Safoglu, *Metall. Trans. A* **6A**, 825–837 (1975)
3. S.H. Goods, L.M. Brown, *Acta Metall.* **27**, 1–15 (1979)
4. Q.-Z. Chen, W.-Y. Chu, Y.-B. Wang, C.-M. Hsiao, *Acta Mater.* **43**, 4371–4376 (1995)
5. R.L. Lyles Jr., H.G.F. Wilsdorf, *Acta Metall.* **23**, 269–277 (1975)
6. A.M. Cuttiño, M. Ortiz, *Acta Mater.* **44**, 427–436 (1996)
7. F.A. McClintock, *Trans. ASME J. Appl. Mech.* **35**, 363–371 (1968)
8. P.F. Thomason, *J. Inst. Metals* **96**, 360–365 (1968)
9. P.F. Thomason, *Acta Metall.* **29**, 763–777 (1981)
10. A.L. Gurson, *Trans. ASME J. Eng. Mater. Tech.* **99**, 2–15 (1977)
11. A.L. Gurson, in *Fracture 1977, Proceedings of The 4th International Conference on Fracture*, vol. 2, ed. by D.M.R. Taplin (University Waterloo Press, Waterloo, 1977), pp. 357–364
12. V. Tvergaard, *J. Mech. Phys. Solids* **30**, 399–425 (1982)
13. A. Needleman, V. Tvergaard, *J. Mech. Phys. Solids* **35**, 151–183 (1987)
14. X. Gao, T. Wang, J. Kim, *Int. J. Solids. Struct.* **42**, 5097–5117 (2005)
15. S. Traiviratana, E.M. Bringa, D.J. Benson, M.A. Meyers, *Acta Mater.* **56**, 3874–3886 (2008)
16. S. Chandra, M.K. Samal, V.M. Chavan, S. Raghunathan, *Phil. Mag.* **98**, 577–604 (2018)
17. M. Nagumo, T. Yagi, H. Saitoh, *Acta Mater.* **48**, 943–951 (2000)
18. H. Yoshida, M. Nagumo, *ISIJ int.* **38**, 196–202 (1998)
19. O.A. Onyewuenyi, in *Hydrogen Degradation of Ferrous Alloys*, ed. by R.A. Oriani, J.P. Hirth, M. Smialowski (Noyes Pub., Park Ridge N.J., 1985), pp. 414–453
20. J.W. Rudnicki, J.R. Rice, *J. Mech. Phys. Solids* **23**, 371–394 (1975)
21. C.D. Beachem, *Metall. Trans.* **3**, 437–451 (1972)
22. R. Kirchheim, *Scr. Mater.* **62**, 67–70 (2010)
23. R. Kirchheim, *Acta Mater.* **55**, 5139–5148 (2007)
24. M.L. Martin, I.M. Robertson, P. Sofronis, *Acta Mater.* **59**, 3680–3687 (2011)
25. K.A. Nibur, B.P. Somerday, D.K. Balch, C. San Marchi, *Acta Mater.* **57**, 3795–3809 (2009)
26. T. Neeraji, R. Srinivasan, J. Li, *Acta Mater.* **60**, 5160–5171 (2012)
27. P. Novak, R. Yuan, B.P. Somerday, P. Sofronis, R.O. Ritchie, *J. Mech. Phys. Solids* **58**, 206–226 (2010)
28. A. Nagao, C.D. Smith, M. Dadfarnia, P. Sofronis, I.M. Robertson, *Acta Mater.* **60**, 5182–5189 (2012)
29. M.L. Martin, B.P. Somerday, R.O. Ritchie, P. Sofronis, I.M. Robertson, *Acta Mater.* **60**, 2739–2745 (2012)
30. Y. Liang, P. Sofronis, N. Aravas, *Acta Mater.* **51**, 2717–2730 (2003)
31. S.P. Lynch, *Acta Metall.* **32**, 79–90 (1984)
32. S.P. Lynch, *Acta Metall.* **36**, 2639–2661 (overview) (1988)
33. O.A. Onyewuenyi, J.P. Hirth, *Metall. Trans. A* **14A**, 259–269 (1983)
34. J.A. Gordon, J.P. Hirth, A.M. Kumar, N.E. Moody Jr., *Metall. Trans. A* **23A**, 1013–1020 (1992)
35. J.P. Hirth, in *Hydrogen Effects on Materials*, ed. by A.W. Thompson, M.R. Moody (TMS, Warrendale PA, 1996), pp. 507–522
36. T.D. Lee, T. Goldenberg, J.P. Hirth, *Metall. Trans. A* **10A**, 439–448 (1979)
37. M. Nagumo, *Mater. Sci. Tech.* **20**, 940–950 (2004)
38. M. Nagumo, K. Takai, *Acta Mater.* **165**, 722–733 (2019)
39. H. Su, H. Toda, R. Masunaga, K. Shimizu, H. Gao, K. Sasaki, M.S. Bhuiyan, K. Uesugi, A. Takeuchi, Y. Watanabe, *Acta Mater.* **159**, 332–343 (2018)
40. M. Nagumo, H. Yoshida, Y. Shimomura, T. Kadokura, *Mater. Trans.* **42**, 132–137 (2001)
41. Y. Ding, H. Yu, M. Lin, K. Zhao, S. Xiao, A. Vinogradov, L. Qiao, M. Ortiz, J. He, Z. Zhang, *Acta Mater.* **239**, 118279 (2022)
42. M. Nagumo, T. Ishikawa, T. Endoh, Y. Inoue, *Scr. Mater.* **49**, 837–842 (2003)
43. A. Harada, K. Kusunoki, K. Moritani, K. Matsumoto, M. Hatano, Y. Horibe, *Philos. Mag. Philos. Mag. Lett.* **101**, 40–50 (2021)